metals

MDPI

Article

Preparation of Bulk TiZrNbMoV and NbTiAlTaV High-Entropy Alloys by Powder Sintering

Yaqi Wu [1], Peter K. Liaw [2] and Yong Zhang [1,*]

[1] State Key Laboratory of Advanced Metals and Materials, University of Science and Technology Beijing, Beijing 100083, China; wuyaqi0223@163.com
[2] Department of Materials Science and Engineering, University of Tennessee, Knoxville, TN 37996, USA; pliaw@utk.edu
* Correspondence: drzhangy@ustb.edu.cn; Tel.: +110-62333073

Abstract: The refractory HEAs block material was prepared by powder sintering, using an equal atomic proportion of mixed TiZrNbMoV and NbTiAlTaV metal powder raw materials. The phase was analyzed, using an XRD. The microstructure of the specimen was observed, employing a scanning electron microscope, and the compressive strength of the specimen was measured, using an electronic universal testing machine. The results showed that the bulk cubic alloy structure was obtained by sintering at 1300 °C and 30 MPa for 4 h, and a small amount of complex metal compounds were contained. According to the pore distribution, the formed microstructure can be divided into dense and porous zones. At a compression rate of $10^{-4}s^{-1}$, the yield strengths of TiZrNbMoV and NbTiAlTaV alloys are 1201 and 700 MPa, respectively.

Keywords: HEAs; hot pressing sintering; microstructure and mechanical behavior; dense and porous

Citation: Wu, Y.; Liaw, P.K.; Zhang, Y. Preparation of Bulk TiZrNbMoV and NbTiAlTaV High-Entropy Alloys by Powder Sintering. *Metals* **2021**, *11*, 1748. https://doi.org/10.3390/met11111748

Academic Editor: Tadeusz Kulik

Received: 7 September 2021
Accepted: 26 October 2021
Published: 31 October 2021

1. Introduction

High-entropy alloys (HEAs) are alloys containing several elements that violate the usual design constraints of one or two alloying components. They are distinguished by multi-component and multi-principal components that combine to produce nanoscale composite materials. [1] The lattice locations of multi-component HEAs are displaced to varying degrees due to the size difference of multi-principal element atoms, resulting in lattice distortion, which significantly enhances the microstructure and characteristics of the alloys [2–4].

In recent years, the study of HEAs has progressed to a new and interesting stage. The study emphasis of HEAs ranges from the crystal structures and mechanical characteristics of HEAs [5], such as hardness, wear resistance, tensile and compressive strengths, to magnetic properties, such as soft magnetic and hard magnetic behavior, magnetic refrigeration, and wave absorption, as well as HEAs film for photo-thermal conversion. Furthermore, the related HEAs preparation technology has been continually improved in response to meet the needs of alloys, and the preparation of eutectic HEAs, for hydrogen storage, high-entropy cemented carbides and coatings, refractory high-entropy alloys (RHEAs), irradiation-resistant HEAs, corrosion-resistant HEAs, and other special properties of HEAs [6–8]. The HEAs preparation and forming technology may also be used to develop a new classification system for HEAs [9], which can be separated into casting HEAs [10,11], thin-film HEAs [12–16], three-dimensionally (3D)-printed [17–19], deformation HEAs [20], powder-metallurgy HEAs [21,22], and numbered based on their phase type. Table 1 lists a few of the numbered alloys.

Vacuum arc melting is generally used to produce high entropy alloys. Although alloy casting has been industrialized, issues such as shrinkage cavity and segregation must still be addressed in the manufacturing and processing of alloys [23]. As a result, the study and development of material preparation technology is equally critical to promoting material

application. Powder metallurgy has recently been used in the preparation of high entropy alloys [24].

The raw material powder is compacted by spark plasma sintering (SPS) and hot-pressing sintering, and an alloy with uniform element distribution and no apparent segregation is produced [21,22]. The general SPS method is utilized in powder metallurgy to produce TaNbVTi series refractory HEAs. SPS with low temperature, short sintering time, and quick cooling speed may produce an alloy with fine grain and uniform structure. Controlling the temperature of SPS improves the strength and form of the alloy, but also limits the size of the produced alloy. Powder sintering can be used to produce the desired form and size of the alloy. By hot pressing and sintering gas atomized powders, Liu et al., [25] created densified FeCoCrNi high entropy alloy bars. The microstructure of the alloy reveals compact, fine, and homogeneous grains, a tensile strength of 750 MPa, an elongation of more than 50%, and mechanical characteristics superior to those of FeCoCrNi HEAs formed by conventional melting [25]. Powder metallurgy typically gets fine powder by mechanical alloying, and the chemical sequence of mechanical alloy is complicated and time-consuming, with contaminants injected into the process.

Table 1. Sorting and numbering of our research group's HEAs.

Number	Alloy Composition	References	Phase
GS101	$Al_{0.3}CoCrFeNi$	[21]	FCC
GS102	$Fe_{28.5}Co_{47.5}Ni_{19}Al_{1.6}Si_{3.4}$	[26]	FCC
GS201	$AlCoCrFeNiTi_{0.2}$	[27]	BCC + B_2
GS202	$W_{0.2}Ta_{0.2}FeCrV$	[12]	BCC
GS203	$Zr_{45}Ti_{31.5}Nb_{13.5}Al_{10}$	[28]	BCC
GS301	$AlCo_{0.4}CrFeNi_{2.7}$	[27]	FCC + B_2

Note: GS is the initial letter of high entropy Chinese; the first number defines the phase structure of the alloy, for example, 1: FCC, 2: BCC, 3: duplex or polyphase; the final two digits reflect the alloy development sequence. Example: the alloy first evolved inside the FCC structure group: GS101.

The benefit of sintering is evident for fcc alloys and elements with low melting points, but it is difficult to produce powder by mechanical alloying and atomization for refractory element powder, such as Ti, Zr, and so on. As a result, after combining high purity element powder, we attempted to produce TiZrNbMoV and NbTiAlTaV HEAs by hot pressing sintering and evaluated the microstructure and mechanical characteristics.

2. Experimental Procedures

Multi-component TiZrNbMoV and NbTiAlTaV HEAs with equal atomic ratio were prepared by mixing high purity metal powder (the purity of 99.9%) with particle size of 10 microns (microstructure are depicted in Figure 1) homogeneously and hot pressing sintering at 30 MPa for 4 h at 1300 °C in high purity argon environment. For all the samples, densities of the sintered bulk alloys were measured by the Archimedes method [29]. The phase composition of the synthesized alloys was investigated by X-ray diffraction (XRD) (see Supplementary Materials) using a Ultima-IV 3 KW (Rigaku Corporation, Tokyo, Japan) diffractometer with Cu K_α radiation. The microstructural investigation was with a Zeiss SUPRA a55 scanning electron microscope (SEM) (Carl Zeiss Microscopy GmbH, Jena, Germany) equipped with the energy-dispersive spectroscopy (EDS). Cylindrical specimens for compressive tests were 5.0 mm in diameter and 10.0 mm in height, and were tested with a WDW-200D electronic universal material testing machine at room temperature under strain rate of $10^{-4}s^{-1}$.

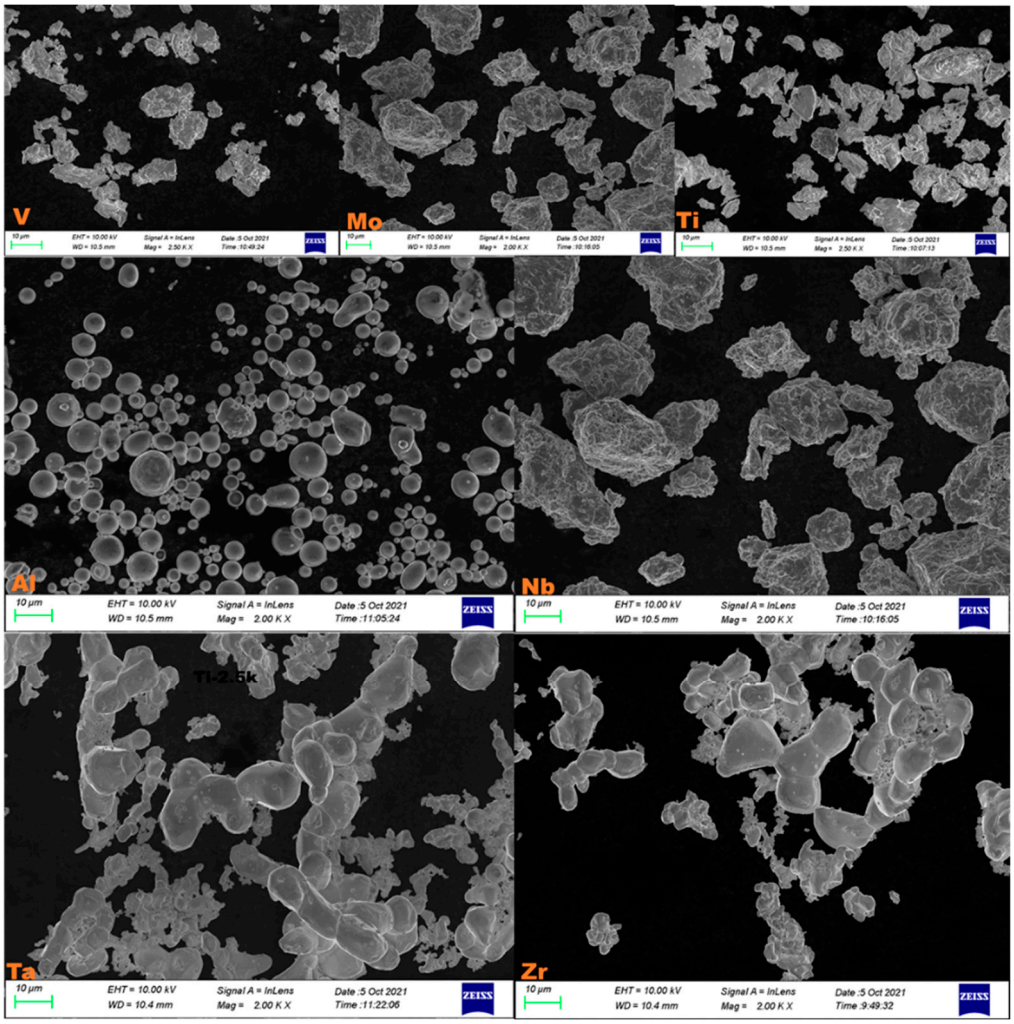

Figure 1. SEM images showing the microstructure of elemental powder.

3. Results

3.1. Crystal Structure and Microstructure

Figure 2 depicts the X-ray diffraction patterns of hot-pressing samples for the TiZrNbMoV and NbTiAlTaV alloys series. The major diffraction peaks are determined to be a typical body centered cubic (BCC) phase. The peak contrast of the XRD diffraction pattern is represented by the positions of the respective peaks of the elements, Ti, Nb, Mo, V, and Ta, and includes several complicated compound peaks, such as AlTa, $AlTi_2$, Mo_9Ti_4, Nb_9Ti_4, and Mo_2Zr, but their intensities are low.

Due to the small amount of metal compounds in the alloy, it cannot be fully detected in the XRD spectrum, according to the analysis. As a result, we used EDS and SEM to further investigate and observe the elemental distribution and microstructure morphology in the alloy.

Figure 3 illustrates representative SEM images of the TiZrNbMoV and NbTiAlTaV alloys, which presents the distribution of ingredients and the phase composition of alloys The elements are not evenly distributed in these alloys, as can be seen, and there are dense and pore zones in the alloy, which would be described by Figure 4.

The results of backscatter indicated that different shades of color represent different element contents. As given in Figure 4a, the main component of Point 1 is the Ti_6Zr_2V compound, the main component of Point 2 would be Nb, and the main component of Point 3 is V. Figure 4b describes that Point 1 is mainly composed of $AlTi_2$ intermetallic

compounds, Point 2 is indeed mainly Nb, and the major element of point 3 is Ta. Point 4 is an AlV_4 intermetallic compound, and the composition is given in Table 2.

Table 2. Chemical composition of different points in TiZrNbMoV and NbTiAlTaV alloys.

Elements-(a)	**Ti-K**	**V-K**	**Zr-K**	**Nb-L**	**Mo-L**
			at.%		
Point 1	62.26	10.11	19.80		7.84
Point 2	1.81	1.95		96.10	
Point 3	0.50	97.75	1.26		0.49
Elements-(b)	**Al-K**	**Ti-K**	**V-K**	**Nb-L**	**Ta-L**
			at.%		
Point-1	31.35	66.74		1.15	0.76
Point-2	0.57			98.16	
Point-3				0.50	97.83
Point-4	17.01	5.06	72.80	3.10	2.04

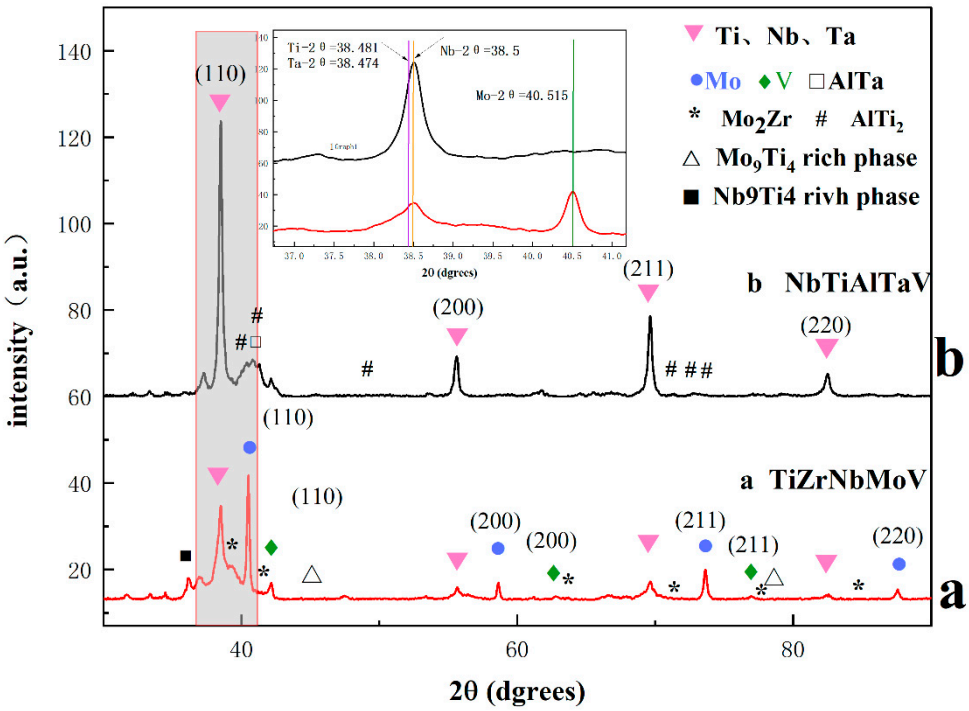

Figure 2. XRD diffraction patterns of the investigated TiZrNbMoV and NbTiAlTaV alloys synthesized, using hot-pressing sintering.

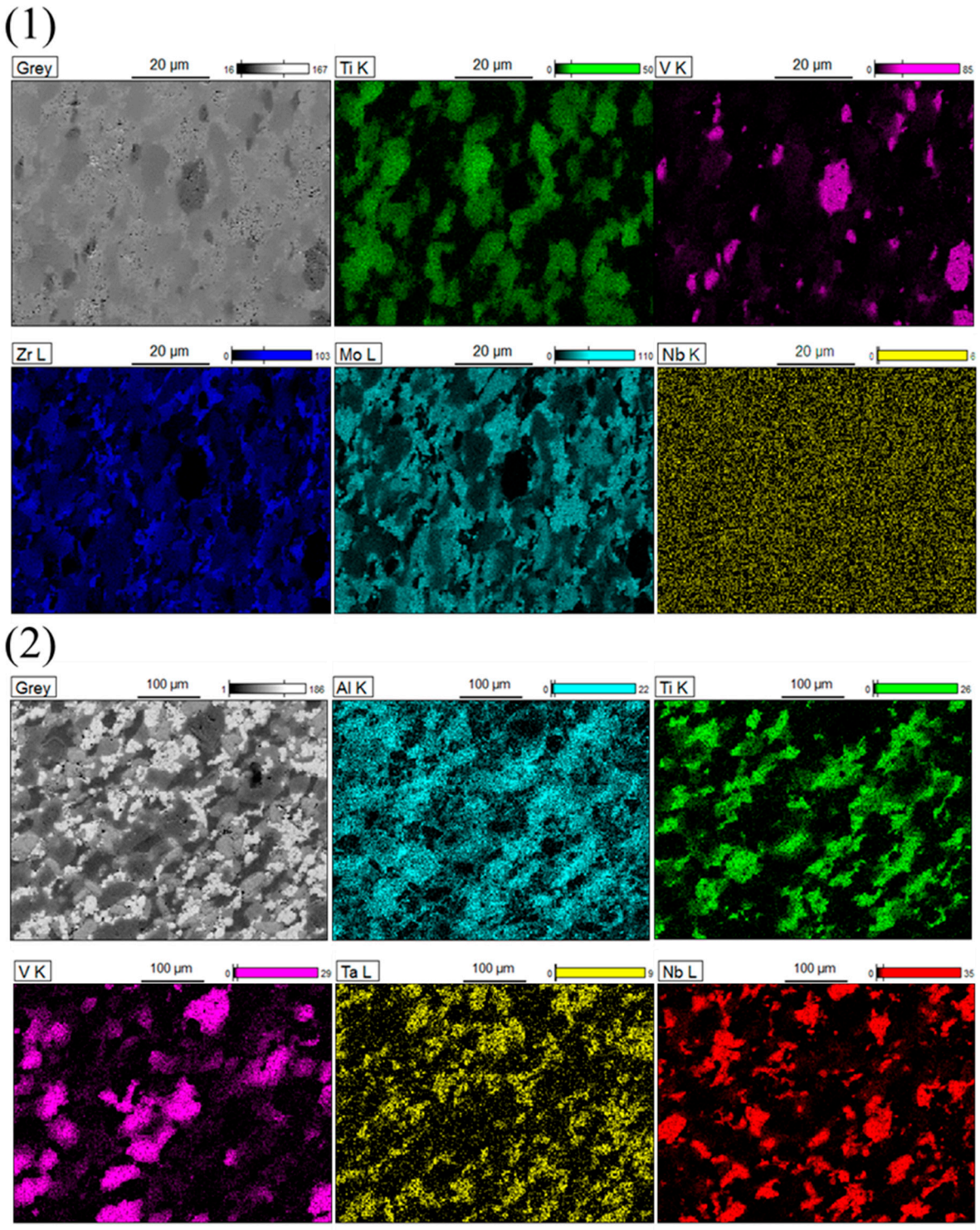

Figure 3. (**1**) EDS analysis of the TiZrNbMoV alloys elemental distribution; (**2**) EDS analysis of the NbTiAlTaV alloys elemental distribution.

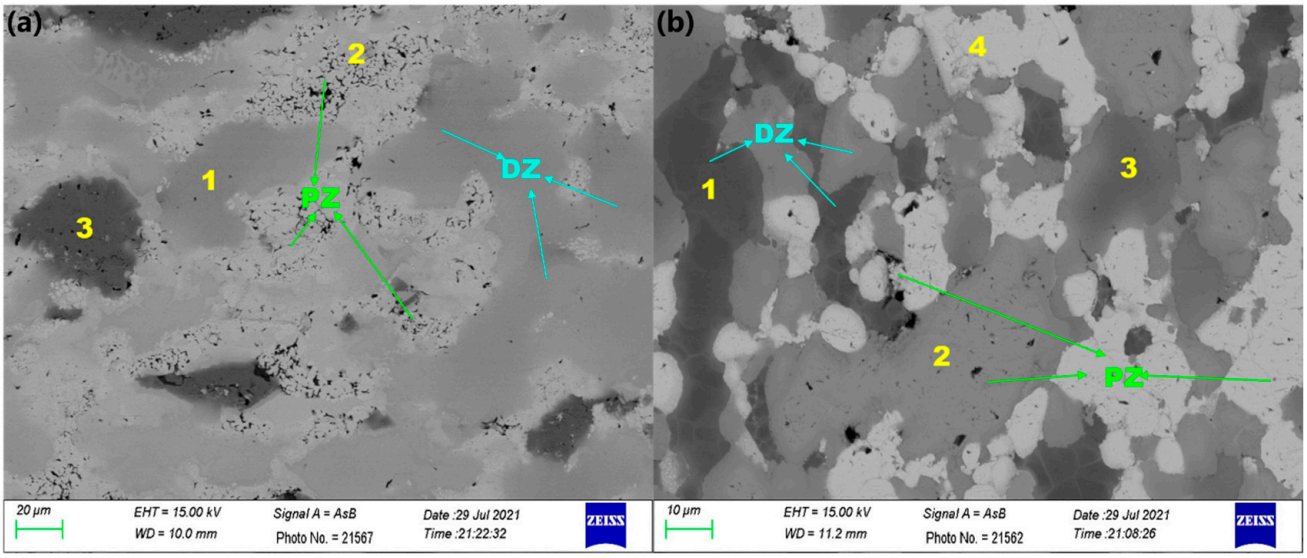

Figure 4. SEM images showing the microstructure morphology of alloys. Image (**a**) is presented for the TiZrNbMoV alloy, (**b**) presents the NbTiAlTaV alloy. DZ: Dense zone; PZ: Porous zone.

3.2. Determination of Porosity

The Archimedes drainage method is used to measure the density of the sample, shown in Equation (1).

$$\rho = \frac{\rho_l m}{m - m_a} \tag{1}$$

where m is the mass of the sample in the air; m_a is the mass measured by the Archimedes drainage method [29]; ρ is the density measured by the Archimedes drainage method; and ρ_l is the density of alcohol, which is 0.789 g/cm^3. Due to the existence of pores in the material structure, alcohol was used in the drainage method for density measurements, which is easy to volatilize, and the sample drying is more convenient to reduce the measurement error.

Before that, the theoretical densities of the samples were calculated as follows: 7.1660 g/cm^3 and 7.8826 g/cm^3, and then the porosity is calculated. The calculation method of porosity is shown in Equation (2).

$$\eta = \left(1 - \frac{\rho}{\rho_{th}}\right) \times 100\% \tag{2}$$

where η (%) is the porosity of the sintered HEAs, ρ (g/cm^3) is the actual density of the measured sample, and ρ_{th} (g/cm^3) is the theoretical density of the sintered HEAs. The data measured by the Archimedes drainage method are shown in Table 3.

Table 3. The density of samples measured by the Archimedes method.

Samples	m/(g)		m_a/(g)		ρ/(g/cm^3)	η(%)
TiZrNbMoV	6.5711 6.5714 6.5712	6.5712	5.8141 5.8140 5.8140	5.8140	6.8476	4.44
NbTiAlTaV	7.1121 7.1119 7.1115	7.1118	6.3582 6.3583 6.3582	6.3582	7.4459	5.54

3.3. Compressive Properties

Figure 5 illustrates the compressive engineering stress–strain curve for alloys under a strain rate $10^{-4}s^{-1}$ at room temperature. Among them, the TiZrNbMoV alloy exhibits a higher yield strength reaching 1201 MPa. In addition, the yield strength of the NbTiAlTaV alloy is 700 MPa. The elastic modulus of these two alloys are 27 and 23 GPa, respectively. Judging from the morphology of the compression fracture SEM images, which are shown in the Figure 6, the compression fracture is a typical brittle fracture with "river-like" or "stair-step" features. This trend is related to the crystal structures of the two alloys. The crystal structures of the two alloys are typical bcc structures. In the bcc crystal structure, the critical stress of the actuating slip system is larger and the number of slip systems is less than FCC, thus it shows the performance characteristics of high strength and low plasticity.

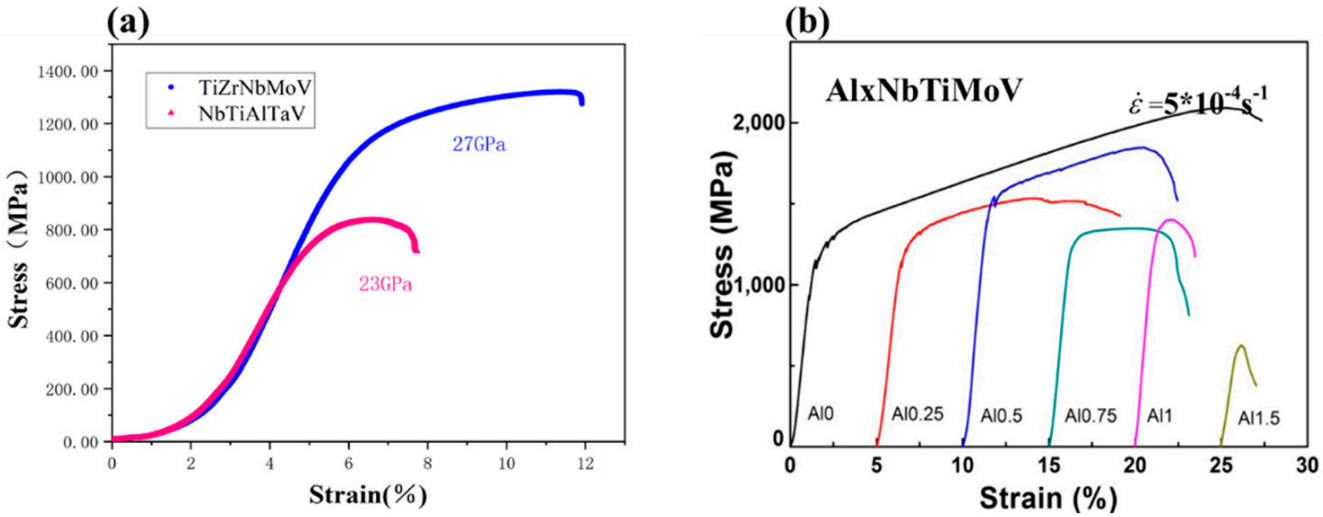

Figure 5. (**a**) Stress-strain curves of TiZrNbMoV and NbTiAlTaV alloys tested at a compression rate of $10^{-4}s^{-1}$. (**b**) Stress-strain curves of $Al_xNbTiMoV$ alloys, data from [30].

The strength of the alloy prepared by hot-pressing sintering is significantly lower when compared to as-cast alloys [30,31]. The analysis of the strength of the hot-pressing sintering state alloy is the main reason for the due to the low preparation temperature of alloy, alloy body internal has not fully alloyed, causing the bonding force between the atoms that make up the elements to be smaller. Furthermore, the scanned fracture surface morphology images in Figure 6 shows that there are many macroscopic pores in the alloy, which are primarily formed by the expansion of air during the sintering process. Figure 7 depicts a schematic representation of the hot-pressing process and the prepared alloy to help you better understand the hot-pressing process. The computer creates the model of Figure 7c using 3D drawing software, so that the alloy produced by hot pressing may be seen more clearly. The real prepared sample is shown in Figure 7d; however, the form of the test sample was supported due to the test need.

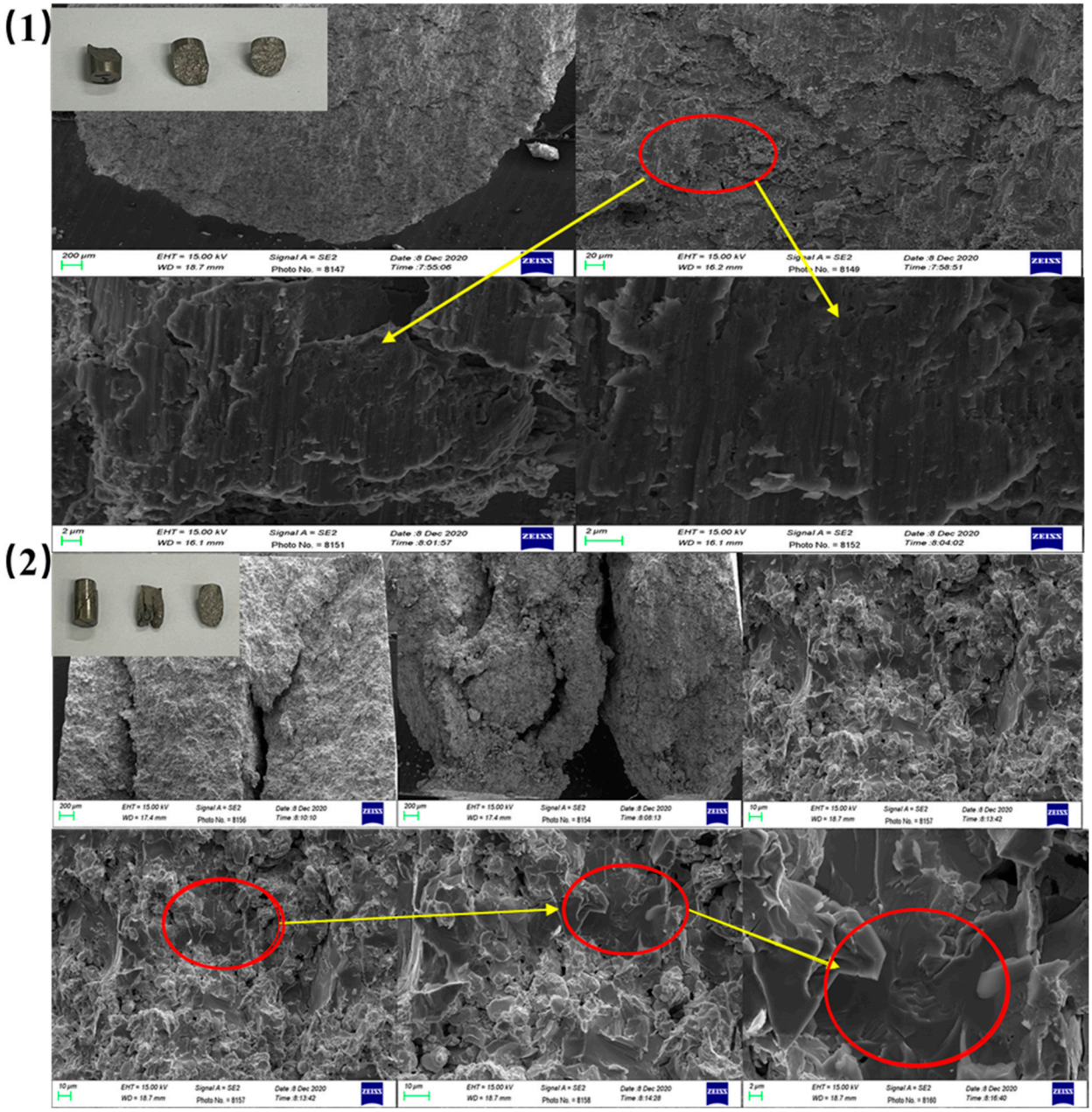

Figure 6. (**1**) Fracture surface images and for the TiZrNbMoV alloys. (**2**) Fracture surface images and for the NbTiAlTaV alloys.

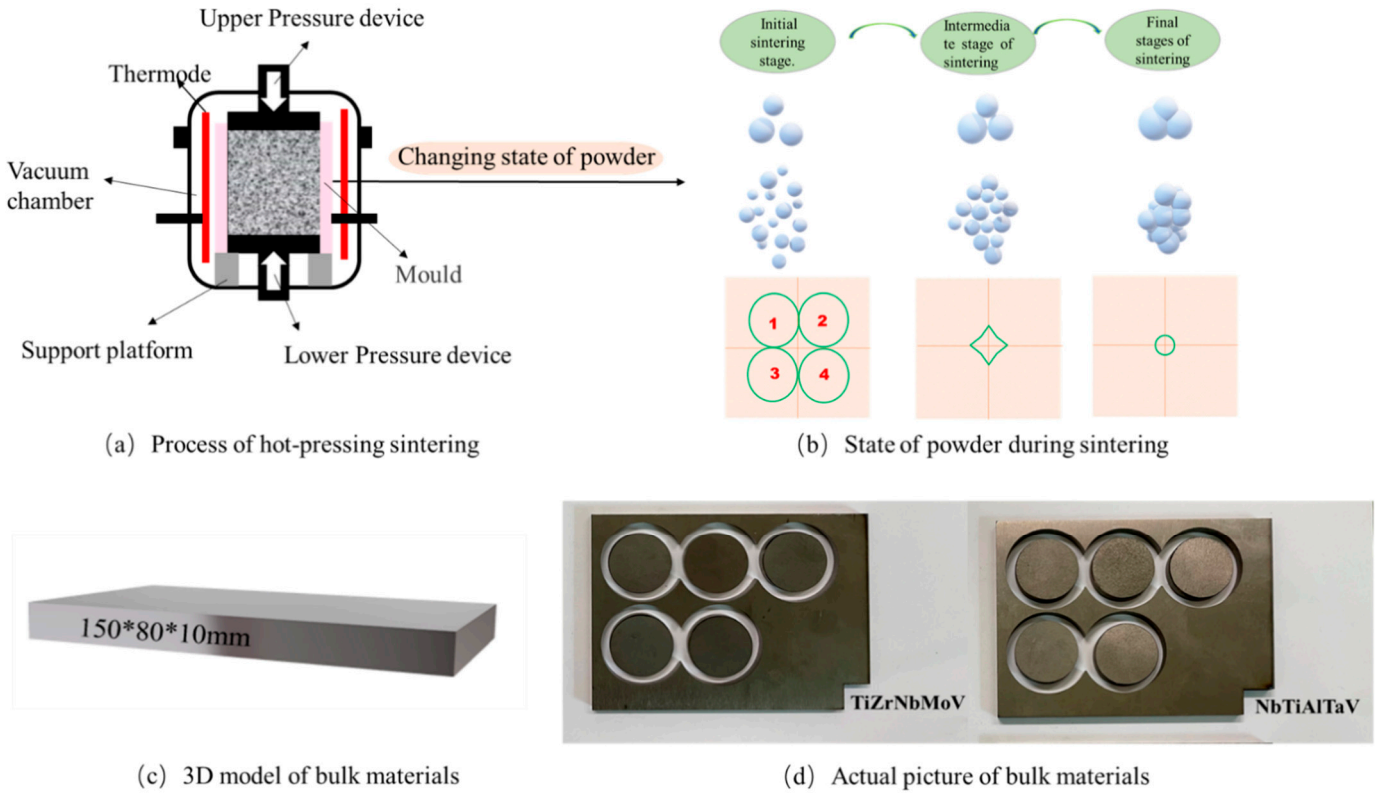

Figure 7. Simple schematic diagram of the sintering process actual picture of bulk materials. (**a**) Process of hot-pressing sintering; (**b**) state of powder during sintering; (**c**) 3D model of bulk materials; (**d**) actual picture of bulk materials.

4. Discussion

In the experimental results, we give the alloys. The phases of the two alloys are mainly typical BCC and a small amount of other compound phases. There are porous and compact areas in the surrounding structure of the alloy. The yield strengths of the two alloys are 1201 and 700 MPa, respectively, and the elastic modulus are 27 and 23 GPa, respectively. These findings contradict assertions that powder metallurgy may generate dense and homogenous alloys. The majority of the refractory elements Ta, Nb, and Mo are agglomerated in the form of elemental in the alloy sintered at 1300 °C. Ti occurs as a body-centered cubic β-Ti phase and as a composite phase with Zr, Al. The goal of sintering metal powder is to produce a solid solution and compound via diffusion. Because the majority of the component elements are refractory elements with high melting points, and melting point of Al is relatively low, and the diffusion ability and rate increase with increasing sintering temperature, Ti-Al, Ta-Al compounds are produced preferentially. The property of Zr, V, on the other hand, is comparable to that of Ti, and a little quantity of solid solution is produced. It is believed that the solid solubility of Ti-Zr-V is low when sintered at 1300 °C, and when cooled in vacuum with the furnace, Zr and V are β stable phases, Ti progressively transforms to α -Ti in the cooling process, and the solid solubility in Ti declines, resulting in a very few solid solution phases. Nevertheless, due to inadequate sintering temperature, Nb, Mo, and Ta tends to produce elemental agglomeration. The microstructure also shows that the majority of the dense regions are composed of compounds and solid solutions generated by elements with low melting points and good diffusion capacity, whereas the holes are composed of elements with high melting points.

An alloy fracture may be defined as the process of crack development, propagation, and fracture. The fracture type of the two alloy groups in the experiment is the same, which belongs to cleavage brittle fracture. The pore region at the surface of the alloy forms stress concentration and microcracks when subjected to external force, and there is no strength

response at the beginning of the stress–strain curve. When the load increases, the stress concentration near the pore tip becomes easier, promoting the crack's quick propagation. Because pores and microcracks already exist throughout the material, when subjected to external stress, the generated microcracks and pores rapidly grow and link from the surface to the interior, resulting in material fracture. As a result, pores and fractures frequently become the fracture source of stress concentration in the pore area, causing the material to fracture at lower stress and reducing strength, plasticity, and toughness.

Our results differ from those achieved with dense, high-strength alloys that are hot-pressed and sintered after the elements are mixed directly with us without prior mechanical alloying. Therefore, the density and mechanical properties are moderate. However, our findings shed some light on the synthesis of sintered high entropy alloys. We discovered that the elastic modulus of the two alloys is similar to that of human bone, and TiZrNb has good biocompatibility [32]. Matching with bone modulus is a required requirement, and too much strength is present, which will prevent explants from adapting in vivo. Therefore, the production of porous materials by hot pressing and sintering element mixture powder opens the door to biomedical alloys. In addition, compared with mechanical alloying and atomized powder metallurgy, hot pressing sintering saves mechanical alloying time, does not introduce impurities in the process of hot pressing sintering, and avoids the danger of atomized powder production.

5. Conclusions

In this article, HEAs of TiZrNbMoV and NbTiAlTaV were created by powder hot-pressing sintering. Structures of bcc phases were discovered in these alloys. Furthermore, alloys had a certain degree of strength, with porosity of 4.44% and 5.54%, respectively. During the sintering process, areas with varying densities and components were produced due to the various spreading abilities of the elements. More research is needed to explore the friction performance and applicability in biomedical materials and self-lubricating materials.

Supplementary Materials: The following are available online at https://www.mdpi.com/article/10.3390/met11111748/s1, Figure S1: Stress-strain curve of AlxTiNbMoV and TiZrNbMoVx alloys (a) and variation of alloy plasticity with V atom ratio (b) [29,30].; Figure S2: XRD patterns of elements labeled with diffraction peaks.; Figure S3: Details of X-ray diffraction spectra of Nb elements.; Figure S4: Details of X-ray diffraction spectra of Ti elements.; Figure S5: Details of X-ray diffraction spectra of Ta elements.; Figure S6: Details of X-ray diffraction spectra of Mo elements.

Author Contributions: Writing—original draft preparation, Y.W.; supervision, Y.Z.; writing—review and editing, P.K.L. All authors have read and agreed to the published version of the manuscript.

Funding: This research was funded by (1) The Guangdong Basic and Applied Basic Research Foundation, grant number No. 2019B1515120020; (2) The State Key Laboratory for Advanced Metals and Materials at the University of Science and Technology Beijing, grant number No. 2020Z-08; (3) The Chinese Funds for Creative Research Groups, grant number No. 51921001; (4) The National Science Foundation, grant number DMR-1611180 and 1809640; (5) the US Army Research Office (W911NF-13-1-0438 and W911NF-19-2-0049).

Institutional Review Board Statement: Not applicable.

Informed Consent Statement: Not applicable.

Data Availability Statement: The data presented in this study are available on request from the corresponding author.

Acknowledgments: Yaqi Wu would like to thank Xuehui Yan and Yasong Li for their assistance with text expression; Yong Zhang is grateful for the funding from (1) the Guangdong Basic and Applied Basic Research Foundation (2019B1515120020), and (2) the State Key Laboratory for Advanced Metals and Materials (2020-Z08) at the University of Science and Technology Beijing 2020Z-08. This work is also funded by the Chinese Funds for Creative Research Groups (No. 51921001). P. K. L. very much appreciates the supports from (1) the National Science Foundation (DMR-1611180 and 1809640)

with program directors, J. Yang, G. Shiflet, and D. Farkas and (2) the US Army Research Office (W911NF-13-1-0438 and W911NF-19-2-0049) with program managers, M.P. Bakas, S.N. Mathaudhu, and D.M. Stepp.

Conflicts of Interest: The author declares no conflict of interest.

References

1. Yeh, J.-W.; Chen, S.-K.; Lin, S.-J.; Gan, J.-Y.; Chin, T.-S.; Shun, T.-T.; Tsau, C.-H.; Chang, S.-Y. Nanostructured High-Entropy Alloys with Multiple Principal Elements: Novel Alloy Design Concepts and Outcomes. *Adv. Eng. Mater.* **2004**, *6*, 299–303. [CrossRef]
2. Qiu, S.; Miao, N.; Zhou, J.; Guo, Z.; Sun, Z. Strengthening mechanism of aluminum on elastic properties of NbVTiZr high-entropy alloys. *Intermetallics* **2018**, *92*, 7–14. [CrossRef]
3. Xu, S.; Zhou, C.; Liu, Y.; Liu, B.; Li, K. Microstructure and mechanical properties of Ti15MoxTiC composites fabricated by in-situ reactive sintering and hot swaging. *J. Alloys Compd.* **2018**, *738*, 188–196. [CrossRef]
4. Coury, F.G.; Kaufman, M.; Clarke, A.J. Solid-solution strengthening in refractory high entropy alloys. *Acta Mater.* **2019**, *175*, 66–81. [CrossRef]
5. Zhang, Y.; Li, R. Editorial for special issue on nanostructured high-entropy materials. *Int. J. Miner. Metall. Mater.* **2020**, *27*, 1309. [CrossRef]
6. Oliveira, J.P.; Shen, J.; Zeng, Z.; Park, J.M.; Choi, Y.T.; Schell, N.; Maawad, E.; Zhou, N.; Kim, H.S. Dissimilar laser welding of a CoCrFeMnNi high entropy alloy to 316 stainless steel. *Scr. Mater.* **2021**, *206*, 114–219. [CrossRef]
7. Martin, A.C.; Oliveira, J.P.; Fink, C. Elemental Effects on Weld Cracking Susceptibility in AlxCoCrCuyFeNi High-Entropy Alloy. *Metall. Mater. Trans. A* **2019**. [CrossRef]
8. Oliveira, J.P.; Curado, T.M.; Zeng, Z.; Lopes, J.G.; Rossinyol, E.; Park, J.M.; Schell, N.; Braz Fernandes, F.M.; Kim, H.S. Gas tungsten arc welding of as-rolled CrMnFeCoNi high entropy alloy. *Mater. Des.* **2020**, *189*, 108505. [CrossRef]
9. Xiaoning, Y.; Weilin, D.; Xiaobo, H.; Linhai, T. Research on preparation methods of high-entropy alloy. *Hot Work. Technol.* **2014**, *43*, 30–33. [CrossRef]
10. Zhou, S.; Liaw, P.K.; Xue, Y.; Zhang, Y. Temperature-dependent mechanical behavior of an Al0.5Cr0.9FeNi2.5V0.2 high-entropy alloy. *Appl. Phys. Lett.* **2021**, *119*, 121902. [CrossRef]
11. Lu, Y.; Zhang, Y.; Guo, S.; Jiang, L.; Kang, H.; Wang, T.; Wen, B.; Wang, Z.; Jie, J.; Cao, Z.; et al. A Promising New Class of High-Temperature Alloys: Eutectic High-Entropy Alloys. *Sci. Rep.* **2014**, *4*, 6200. [CrossRef]
12. Zhang, W.; Liaw, P.K.; Zhang, Y. A Novel Low-Activation VCrFeTaxWx (x = 0.1, 0.2, 0.3, 0.4, and 1) High-Entropy Alloys with Excellent Heat-Softening Resistance. *Entropy* **2018**, *20*, 951. [CrossRef]
13. Khan, N.A.; Akhavan, B.; Zhou, H.; Chang, L.; Wang, Y.; Sun, L.; Bilek, M.M.; Liu, Z. High entropy alloy thin films of $AlCoCrCu_{0.5}FeNi$ with controlled microstructure. *Appl. Surf. Sci.* **2019**, *495*, 143560. [CrossRef]
14. Zhang, Y.; Yan, X.; Ma, J.; Lu, Z.; Zhao, Y. Compositional gradient films constructed by sputtering in a multicomponent TiAl(Cr, Fe, Ni) system. *J. Mater. Res.* **2018**, *33*, 3330–3338. [CrossRef]
15. Xing, Q.; Ma, J.; Zhang, Y. Phase thermal stability and mechanical properties analyses of (Cr,Fe,V)(Ta,W) multiple-based elemental system using a compositional gradient film. *Int. J. Miner. Metall. Mater.* **2020**, *27*, 1379–1387. [CrossRef]
16. Firstov, S.A.; Gorban, V.F.; Danilenko, N.I.; Karpets, M.V.; Andreev, A.A.; Makarenko, E.S. Thermal stability of superhard nitride coatings from high entropy multicomponent TiVZrNbHf alloy. *Powder Metall. Met. Ceram.* **2014**, *52*, 560–566. [CrossRef]
17. Lai, C.; Cheng, K.; Lin, S.; Yeh, J. Mechanical and tribological properties of multi-element (AlCrTaTiZr)N coatings. *Surf. Coat. Technol.* **2008**, *202*, 3732–3738. [CrossRef]
18. Murr, L.E.; Martinez, E.; Amato, K.N.; Gaytan, S.M.; Hernandez, J.; Ramirez, D.A.; Shindo, P.W.; Medina, F.; Wicker, R.B. Fabrication of metal and alloy components by additive manufacturing: Examples of 3D materials science. *J. Mater. Res. Technol.* **2012**, *1*, 42–54. [CrossRef]
19. Li, R.; Niu, P.; Yuan, T.; Cao, P.; Chen, C.; Zhou, K. Selective laser melting of an equiatomic CoCrFeMnNi high-entropy alloy: Processability, non-equilibrium microstructure and mechanical property. *J. Alloys Compd.* **2018**, *746*, 125–134. [CrossRef]
20. Brif, Y.; Thomas, M.; Todd, I. The use of high-entropy alloys in additive manufacturing. *Scr. Mater.* **2015**, *99*, 93–96. [CrossRef]
21. Li, D.; Li, C.; Feng, T.; Zhang, Y.; Sha, G.; Lewandowski, J.J.; Liaw, P.K.; Zhang, Y. High-entropy Al0.3CoCrFeNi alloy fibers with high tensile strength and ductility at ambient and cryogenic temperatures. *Acta Mater.* **2017**, *123*, 285–294. [CrossRef]
22. Lukac, F.; Dudr, M.; Musalek, R.; Klecka, J.; Cinert, J.; Cizek, J.; Chraska, T.; Cizek, J.; Melikhova, O.; Kuriplach, J.; et al. Spark plasma sintering of gas atomized high-entropy alloy HfNbTaTiZr. *J. Mater. Res.* **2018**, *33*, 1–11. [CrossRef]
23. Cao, Y.; Liu, Y.; Liu, B.; Zhang, W. Precipitation behavior during hot deformation of powder metallurgy Ti-Nb-Ta-Zr-Al high entropy alloys. *Intermetallics* **2018**, *100*, 95–103. [CrossRef]
24. Liu, Y.; Cao, Y.-k.; Wu, W.-q.; Song, M.; Zhang, W.; Liu, B. Progress of powder metallurgical high entropy alloys. *Chin. J. Nonferrous Met.* **2019**, *9*, 2155–2184. [CrossRef]
25. Liu, B.; Wang, J.; Liu, Y.; Fang, Q.; Chen, S.; Liu, C.T. Microstructure and mechanical properties of equimolar FeCoCrNi high entropy alloy prepared via powder extrusion. *Intermetallics* **2016**, *75*, 25–30. [CrossRef]
26. Zhang, M.; Zhang, Y.; Li, D.; Zuo, T.; Zhou, K.; Gao, M.; Sun, B.; Shen, T. Metals Compositional Design of Soft Magnetic High Entropy Alloys by Minimizing Magnetostriction Coefficient in $(Fe_{0.3}Co_{0.5}Ni_{0.2})_{100-x}(Al_{1/3}Si_{2/3})_x$ System. *Metals* **2019**, *9*, 382. [CrossRef]

27. Zhang, L.; Zhang, Y. Tensile Properties and Impact Toughness of AlCoxCrFeNi$_{3.1-x}$(x=0.4,1) High-Entropy Alloys. *Front. Mater.* **2020**, *7*, 92. [CrossRef]
28. Yan, X.; Zhang, Y. Utrastrong and ductile BCC high-entropy alloys with low-density via dislocation regulation and nanoprecipitates. *JMST*. submitted.
29. Chen, S.Y.; Yang, X.; Dahmen, K.A.; Liaw, P.K.; Zhang, Y. Microstructures and Crackling Noise of Al$_x$NbTiMoV High Entropy Alloys. *Entropy* **2014**, *16*, 870–884. [CrossRef]
30. Zhang, Y.; Yang, X.; Liaw, P.K. Alloy Design and Properties Optimization of High-Entropy Alloys. *JOM* **2012**, *64*, 830–838. [CrossRef]
31. Yan, X.; Zhang, Y. A body-centered cubic Zr50Ti35Nb15 medium-entropy alloy with unique properties. *Scr. Mater.* **2020**, *178*, 329–333. [CrossRef]
32. *Porous Materials for Powder Metallurgy*; Metal Research Institute (Ed.) Metallurgical Industry Press: Beijing, China, 1979. [CrossRef]